

Submitted to Astrophysical Journal

Ultraviolet observations of the X-ray photoionized wind of Cygnus X-1 during X-ray soft/high state¹

S. D. Vrtilek², B.S. Boroson², A. Hunacek³, D. Gies⁴, C. T. Bolton⁵

¹*Harvard-Smithsonian Center for Astrophysics, 60 Garden Street, Cambridge, MA 02138,*

²*Department of Physics, MIT, 77 Massachusetts Avenue, Cambridge, MA 02139,* ³*Center for High Angular Resolution Astronomy, Department of Physics and Astronomy, Georgia State University, P. O. Box 4106, Atlanta, GA 30302-4106,* ⁴*David Dunlap Observatory, University of Toronto, P.O. Box 360, Richmond Hill, Ontario, L4C 4Y6; Canada*

svrtilek@cfa.harvard.edu

ABSTRACT

High-resolution ultraviolet observations of the black hole X-ray binary Cygnus X-1 were obtained using the Space Telescope Imaging Spectrograph on the Hubble Space Telescope. Observations were taken at two epochs roughly one year apart; orbital phase ranges around $\phi_{orb} = 0$ and 0.5 were covered at each epoch. We detect P Cygni line features from high (N V, C IV, Si IV) and absorption lines from low (Si II, C II) ionization state material. We analyze the characteristics of a selection of P Cygni profiles and note, in particular, a strong dependence on orbital phase for the high ionization material: the profiles show strong, broad absorption components when the X-ray source is behind the companion star and noticeably weaker absorption when the X-ray source is between us and the companion star.

We fit the P Cygni profiles using the Sobolev with Exact Integration method applied to a spherically symmetric stellar wind subject to X-ray photoionization from the black hole. Of the wind-formed lines, the Si IV doublet provides the most reliable estimates of the parameters of the wind and X-ray illumination. The

¹Based on observations with the NASA/ESA Hubble Space Telescope obtained at the Space Telescope Science Institute, which is operated by the Association of Universities for Research in Astronomy, Incorporated, under NASA contract NAS5-26555. These observations are associated with programs GO-9646 and GO-9840.

velocity v increases with radius r (normalized to the stellar radius) according to $v = v_\infty(1 - r_*/r)^\beta$, with $\beta \approx 0.75$ and $v_\infty \approx 1420 \text{ km s}^{-1}$. The microturbulent velocity was $\approx 160 \text{ km s}^{-1}$. Our fit implies a ratio of X-ray luminosity (in units of $10^{38} \text{ erg s}^{-1}$) to wind mass-loss rate (in units of $10^{-6} M_\odot \text{ yr}^{-1}$) of $L_{X,38}/\dot{M}_{-6} \approx 0.33$, measured at $\dot{M}_{-6} = 4.8$. The lines from the lower ionization species and the He II $\lambda 1640$ absorption are consistent with formation in the photosphere of the normal companion.

Our models determine parameters that may be used to estimate the accretion rate onto the black hole and independently predict the X-ray luminosity. Our predicted L_x matches that determined by contemporaneous RXTE ASM remarkably well, but is a factor of 3 lower than the rate according to Bondi-Hoyle-Littleton spherical wind accretion. We suggest that some of the energy of accretion may go into powering a jet.

Subject headings: black holes binaries: individual (Cyg X-1)—ultraviolet: stars—X-rays: winds

1. Introduction

Cygnus X-1, the only Galactic X-ray binary with a high mass companion where existing observations require a black hole for the compact object, was first discovered in 1962 (Cowley 1992, and references therein). In addition to the well-established high mass function found with optical observations, the X-ray data of Cyg X-1 display transitions from a high flux state in the 2-10 keV band (where a strong soft component dominates) to a low flux state (where the soft component largely disappears) that has been interpreted as characteristic of black hole systems. It also displays highly broadened Fe $K\alpha$ emission (Miller *et al.* 2002) that is consistent with models for X-ray reflection in Galactic black holes and AGNs. The broad-line shape of Fe $K\alpha$ may be caused by Doppler shifts and the gravitational field of the black hole.

The Cyg X-1 system consists of a supergiant star and a compact object. The mass of the compact object is in the range 7-20 M_\odot (Shaposhnikov & Titarchuk 2007; Ziolkowski 2005) the mass of the visible star is in the range 18-40 M_\odot (Ziolkowski 2005; Tarasov *et al.* 2003; Brocksopp *et al.* 1999). The binary orbital period is 5.6 days (Bolton 1972). Miller *et al.* (2005) using Chandra/HETG observations find that the X-ray spectrum of Cygnus X-1 at phase 0.76 is dominated by absorption lines, in strong contrast to spectra of other HMXBs such as Vela X-1 and Cen X-3. Schulz *et al.* (2002) report marginal evidence for ionized Fe transitions with P-Cygni type profiles at orbital phase 0.93 whereas Marshall *et al.* (2001) find no

evidence for such line profiles at phase 0.84. Miller *et al.* (2005) suggest that, while the spectra of Cen X-3 can be modelled by a spherically-symmetric wind (Wojdowski *et al.* 2003), the X-ray absorption spectrum of Cyg X-1 requires dense material preferentially along the line of sight; considered together, the Chandra spectra provide evidence in X-rays for a focused wind in Cygnus X-1.

Our Space Telescope Imaging Spectrometer (STIS) observations of Cygnus X-1 were obtained when Cyg X-1 was in its soft/high X-ray state and show line profiles that change significantly between orbital phases 0.0 and 0.5. We interpret these changes in terms of models that include the effects of X-ray photoionization on the stellar wind of the normal companion or of a focused wind. We test our model predictions with contemporaneous X-ray observations. The observations and analysis are described in Section 2, our models of the line profiles are presented in Section 3, and our interpretation and conclusions are discussed in Section 4.

2. Observations and Analysis

Cyg X-1 was observed with the STIS on the Hubble Space Telescope (HST) when the X-ray source was behind the normal star and half an orbit later on two separate epochs roughly one year apart. Figure 1 shows the times of our observations in comparison with the 1 day-averaged light curves obtained from the all-sky monitor on the Rossi X-Ray Timing Explorer (RXTE; Levine *et al.* 1996). The RXTE light curves show that the HST observations were taken when the binary was at relatively high X-ray flux which is associated with the X-ray soft/high state.

The STIS instrument design and in-orbit performance have been described by Woodgate *et al.* (1998) and Kimble *et al.* (1998). The E140M grating provided a resolving power of 6 km s^{-1} in the wavelength range 1150–1740 Å. The data were processed through the standard HST/STIS pipeline and further reduced using the STSDAS routines available through IRAF.

Table 1 lists the HST observation identifier, along with the start dates, exposure length, and orbital phase at the start of each observation. Phases were calculated using an ephemeris that places phase zero at $\text{JD}2441874.707 \pm 0.009$, with an orbital period of 5.599829 ± 0.000016 (Brocksopp *et al.*, 1999). Phase zero corresponds to supergiant inferior conjunction.

Figure 2 shows the eight datasets in increasing orbital phase order regardless of epoch. These data are not smoothed and not corrected for reddening and no instrumental quality control has been applied (i.e., removal of hot pixels, etc). It is clear that the changes in high

ionization material line profiles are orbital phase dependent, with stronger absorption near orbital phase 0.0. The close-ups of the N V, Si IV, and C IV regions in Figure 3 demonstrate that this orbital phase dependence persists for observations taken a year apart.

Figure 4 shows a spectrum taken at orbital phase 0.96, with the stronger spectral lines labeled. Table 2 lists the features identified using the program SpecView ¹ and tables supplied by NIST ². We note that some of the lines are saturated and several are blended with other features. Figures 5-10 show profiles of both high (N V, C IV, Si IV) and low (Si II, C II) ionization state material in each of two orbital phases at two epochs. The low ionization material and He II are likely to be from the stellar surface rather than the wind.

3. Line Profile Models

We have implemented a model that uses the Sobolev method with Exact Integration (SEI; Lamers *et al.* 1987) to predict the P Cygni line profiles from a wind ionized by an embedded X-ray source. The details of the wind ionization are identical to those given by Boroson *et al.* (1999; equations 11-16). The SEI method extends the escape probability method of McCray *et al.* (1984) by including integration along the line of sight. This allows scattering from a range of points around the “resonant point”, as will result when there is small-scale turbulence (microturbulence). The SEI method also allows a more exact treatment of interaction between P Cygni line doublet components.

We take note of a complementary analysis of the same STIS observations by Gies *et al.* (2007). Gies *et al.* also use the SEI method to analyze the wind, but assume that the ions that form the P Cygni lines are *only* present in the region of the wind in which the primary blocks X-ray ionization from the black hole.

Following McCray *et al.* (1984), we compute the local ionization fraction by combining ambient photoionization (from shocks in the wind, etc.) that would be present in an isolated O star with the ionization rate computed using the XSTAR code, assuming a local ionization parameter $\xi = L_x/nr_x^2$ (with X-ray luminosity L_x , number density n , and distance from the black hole r_x). We use the X-ray spectrum shape modeled by Wilms *et al.* (2006) for observations taken near our HST observations. Where the O star shadows the wind from X-ray photoionization by the black hole, we assume only the ambient photoionization rate,

¹http://www.stsci.edu/resources/software_hardware/specview

²<http://www.physics.nist.gov/PhysRefData/Handbook/index.html>

which gives optical depths in the line parameterized by α_1 and α_2 , or τ_{wind} , often used for winds of isolated OB stars (Lamers *et al.* 1987). The XSTAR ionization code is described in Bautista & Kallman (2001).

We fit the model, which includes adjustable free parameters, to the spectra at phases near both superior and inferior conjunction of the black hole. Thus, the fits are sensitive to both the blue-shifted absorption trough and the red-shifted emission peak. Although the lines are saturated, the optical depths of the lines in the absence of X-ray photoionization still affect the resultant fits.

We attribute the sharp features (velocity widths of order 30 km s^{-1}) to interstellar absorption lines, the narrow absorption lines (widths of 94 km s^{-1}) originate on the stellar photosphere, and the broadest features come from the wind (terminal velocity from our model of 1420 km s^{-1}). In addition, when we model the NV lines, we incorporate narrow interstellar Mg II lines at 1239.925, 1240.397 Å. The SEI calculation of the line profiles near the rest velocity can require integration to start extremely close to the stellar surface in order to agree with the results of comoving frame methods (Lamers *et al.* 1987). Hence we expect the P Cygni line fits to be least reliable near the rest wavelengths of the lines.

We assumed fixed values for parameters describing the O star and orbit as given in Table 3. Our results are not sensitive to the abundance values used, except for the determination of \dot{M} . The parameters describing the wind and X-ray illumination are allowed to vary until a χ^2 minimum is found through the downhill simplex (“amoeba”) method of Nelder & Mead (1965). The errors we quote are the rms variation in the final simplex, in which the χ^2_ν varies by less than 1%. There may be other local χ^2 minima and some of the parameters may interact. For example, different values of τ_{wind} , α_1 , α_2 may produce similar functions of optical depth versus radius in the wind.

The Si IV doublet is generally the most reliable indicator of wind behavior in stars of this spectral type (Lamers *et al.* 1999), as the NV and CIV lines are saturated. We show that the lines can be fit using a wind acceleration law that is standard for OB stars: $v = v_\infty(1 - 1/r)^\beta$, with r the radius in the wind normalized to the stellar radius, and v_∞ and β free parameters of our model. (We note that our code used $v = 0.01v_\infty + 0.99*v_\infty(1 - 1/r)^\beta$ in order to avoid singularities). The best-fit value of β is ≈ 0.75 , which is standard for OB star winds. The best-fit value of $v_\infty \approx 1420 \text{ km s}^{-1}$ is lower than the 2300 km s^{-1} found by Davis & Hartmann (1983). It is possible that the higher terminal velocity found by Davis & Hartmann was due to line blending on the blue side of the feature that was hard to discern in the weak IUE spectrum. We also note that Davis & Hartmann used IUE data of mostly C IV to determine their terminal velocity whereas we use STIS data of Si IV. Also we allow for microturbulence. For the CIV lines we fix β to that found for the Si IV fits, and then for

NV, which has a lower signal to noise ratio, we fix also v_∞ . The best-fit parameters for the fits shown in Figures 11-13 are given in Table 4.

4. Accretion Rate and X-ray Luminosity

4.1. Mass Accretion Rate

The fits to the changing P Cygni lines by a model of X-ray ionization within a spherically symmetric wind determine parameters that may be used to estimate the accretion rate onto the black hole. For accretion purely through capture of stellar wind material, Bondi & Hoyle (1944) show that the rate at which mass is captured from a stellar wind by a compact object (\dot{M}_{capture}) is given by

$$\dot{M}_{\text{capture}} = \frac{4\pi G^2 M_{\text{bh}}^2 \rho}{V_{\text{rel}}^3} \quad (1)$$

where G is the gravitational constant, M_{bh} is the mass of the compact object, ρ is the density of the undisturbed gas flow near the compact object, and $V_{\text{rel}} = (v_{\text{wind}}^2 + v_{\text{orbit}}^2)^{1/2}$ is the velocity of the wind relative to the compact object, which has velocity $v_{\text{orbit}} = 2\pi R/P$ for orbital radius R and period P in a wind we take to have $v_{\text{wind}} = v_\infty(1 - R_*/R)^\beta$. From mass conservation we have

$$\rho = \frac{\dot{M}}{4\pi R^2 v_{\text{wind}}} \quad (2)$$

We can relate \dot{M}_{capture} to the X-ray luminosity if we assume accretion releases energy with some efficiency $e \approx 0.1$, so that $L_x = e\dot{M}_{\text{capture}}c^2$. For disk accretion, we expect $e = 0.057$ for a nonrotating black hole and $e = 0.42$ for a maximally rotating black hole (Shapiro & Teukolsky 1983, p. 429).

Thus our best-fit values for \dot{M} , β , and v_∞ provide an independent prediction of L_x . This prediction is based on the idealization that the accretion proceeds entirely through the gravitational capture of stellar wind material. The prediction also depends on other uncertain parameters (e , M_{bh}). Our estimate, $L_x \approx 8 \times 10^{37} \text{ erg s}^{-1}$ depends sensitively on the velocity of the stellar wind near the black hole. As v_∞ varies from 1000 to 2000 km s^{-1} , L_x goes from 3×10^{37} to $3 \times 10^{38} \text{ erg s}^{-1}$.

The model dependence on the properties of the X-ray ionized region of the wind also leads to a determination of L_x/\dot{M} and \dot{M} , which together give $L_x = 1.6 \times 10^{37} \text{ erg s}^{-1}$ and $\dot{M} = 4.8 \times 10^{-6} M_\odot \text{ yr}^{-1}$ in the fit to the SiIV lines. The CIV and NV lines, which we expect to be less reliable, give $L_x = 1.8 \times 10^{38}$ and $L_x = 8.0 \times 10^{37} \text{ erg s}^{-1}$, respectively.

We can compare these models for the X-ray luminosity with the observed contemporaneous RXTE ASM count rate, $\approx 80 \text{ counts s}^{-1}$ (Figure 1). Schulz et al. (2002) observed Cygnus X-1 with *Chandra* during a period in which the RXTE ASM showed flares. An upper estimate for the ASM count rate during their observation, $\approx 50 \text{ cts s}^{-1}$, together with their measure of the 0.5-10 keV X-ray luminosity as $1.6 \times 10^{37} \text{ erg s}^{-1}$ (for a distance of 2.5 kpc), would imply an X-ray luminosity of $\geq 2.6 \times 10^{37} \text{ erg s}^{-1}$ during the STIS observations.

4.2. X-ray Luminosity

One further uncertainty in our model of the wind is that we assume a constant X-ray luminosity whereas the X-rays from Cygnus X-1 often flare and display a complex power spectrum. The saturated P Cygni lines may respond nonlinearly to flares, although light travel times may diminish the response. In Figures 14 and 15, we show how the P Cygni lines may change in our model in response to a change in X-ray luminosity. If the change were linear, the graph of the model with best-fit value of L_x would be identical to the average of the other two graphs. Whereas we see a clear asymmetry.

In Figures 16, 17, and 18, we show contours of constant values of $\text{Log}_{10}(a_{\text{SiIV}})$, where a_{SiIV} is the fraction of Si that is in the form SiIV. The lines extending radially from the center of the O star show the lines of sight at $\phi = 0.55$ (extending to the bottom) and $\phi = 0.96$ (extending to the top), adjusted for orbital inclination i by the use of an effective phase ϕ' such that $\cos 2\pi\phi' = \cos 2\pi\phi \sin i$.

Figures 16 through 18 show that the black hole is very effective at removing the SiIV ion from the wind. However, it is difficult to see intuitively the optical depth in the wind, given the ion fraction. Therefore, we show in Figures 19 through 21 the radial optical depths of SiIV in the wind, given the same three X-ray luminosities, $L_x = (1/3, 1, 5/3) \times 1.6 \times 10^{37} \text{ erg s}^{-1}$, with other parameters fixed to the best-fit values. From these plots it should be apparent that the global ionization in the wind is sensitive to the X-ray luminosity. This is particularly true at the low end of the X-ray luminosity range. In that case, a large region outside of the X-ray shadow remains at an optical depth that causes noticeable signatures in the line profiles, in spite of X-rays from the black hole.

In these figures, we use our parameterization of the background optical depth in terms of α_1 , α_2 , and τ_{wind} to determine the optical depth in the shadow region. The resulting contours of constant optical depth are ellipsoidal, compacted towards the compact object.

5. Discussion and Conclusions

The Space Telescope Imaging Spectrograph on Hubble provides the highest resolution ultraviolet spectra taken of Cyg X-1 to date. Observations were taken at two epochs roughly a year apart: at each epoch orbital phases when the compact object is behind the stellar companion and when the compact object is in front of the companion star were covered. We find P Cygni profiles from high ionization (NV, CIV, SiIV) gas. For both epochs the P Cygni profiles show significantly less absorption at phases when the compact object is in the line of sight. RXTE observations indicate that the X-ray flux of the system was at a similar level at each epoch. The observed changes can be attributed entirely to orbital effects. We interpret this to mean that X-rays from the compact object photoionize the wind from the massive companion resulting in reduced absorption by the wind material.

P Cygni profiles of selected species are consistent with the Hatchett-McCray effect, in which X-rays from the compact object photoionize the stellar wind from the companion star, thereby reducing absorption. This effect also appears in UV observations of LMC X-4 and SMC X-1 (Boroson *et al.* 1999; Vrtilik *et al.* 1997; Treves *et al.* 1980). SEI models can fit the observed P Cygni profiles and provide measurements of the stellar wind parameters. The SiIV fits are the most reliable and we use them to determine $L_x/\dot{M} = 4.8 \pm 0.3 \times 10^{42}$ ergs s⁻¹ M_☉⁻¹ yr, where L_x is the X-ray luminosity and \dot{M} is the mass-loss rate of the star. The results from the CIV and NV lines are less reliable because they are saturated and the CIV fit does not match the data well. For these fits we fixed the terminal velocity ν_∞ and the microturbulent velocity to those given by our fits to SiIV.

The best fit values for the optical depth in the ambient wind are high (≥ 10). Once saturated, the OB star wind lines hardly change with large optical depth, but when much of the wind is ionized by the black hole, the ion fraction in the remaining regions can have a significant effect on the line profile.

The reduced absorption when the compact object is in the line of sight is inconsistent with focusing of the wind toward the compact object, as has been suggested by several authors (e.g, Sowers *et al.* 1998; Tarasov *et al.* 2003; Miller *et al.* 2005), as then we would expect more absorbers in the line-of-sight and hence increased P Cygni absorption. Also, IUE observations taken at 8 orbital phases show a continuous variation in the P Cygni profiles with maximum absorption at phase 0.0 and minimum at 0.5 (Treves *et al.* 1980; van Loon *et al.* 2001). Further high spectral resolution ultraviolet observations of Cyg X-1 will be necessary to study the behavior of the P Cygni lines during different X-ray states.

In an analysis of 2 years of RXTE/ASM data Wen *et al.* (1999) found the 5.6 day orbital period of Cyg X-1 during the X-ray low/hard state, but no evidence of the orbital period

during the high/soft state. Wen *et al.* suggest that absorption of X-rays by a stellar wind from the companion star can reproduce the observed X-ray orbital modulations in the hard state: The lack of modulation in the soft state could be due either to a reduction of the wind density during the soft state or to partial covering of a central hard X-ray emitting region by an accretion stream. Gies *et al.* (2003) used the results of a four year spectroscopic monitoring program of the H α emission strength of HDE226868, the normal companion to Cyg X-1, to argue that the low/hard X-ray state occurs when there is a strong, fast wind and accretion rate is low, while in the high/soft state a weaker, highly ionized wind attains only a moderate velocity and the accretion rate increases. The interpretations of both Wen *et al.* (1999) and Gies *et al.* (2003) are inconsistent with the fact that the *total* X-ray luminosity from 1.3-200 keV remains constant during both the X-ray soft and hard states (Wen *et al.* 1999): the designation of X-ray high or X-ray low during these states is only applicable for the 1.5-12 keV ASM band. Since the 1.3-200 keV X-ray luminosity is unchanged from the hard to soft state, fluctuations in the narrow ASM band cannot be due to reduction in accretion, or obscuration of the X-ray source; rather it is a physical change that causes the dominant emission mechanism to switch from thermal to power-law.

We note that the orbital modulation observed by Wen *et al.* in the hard state (± 1.6 ASM cts/sec around the average) is less than the errors on the counts during the soft state (± 3 ASM cts/sec); we suggest that the quality of the RXTE ASM is not sufficient to detect this low level orbital modulation during the soft state. Ultraviolet observations clearly show orbital modulation during both X-ray hard and soft states (Gies *et al.* 2007). Our wind models explain both the X-ray and ultraviolet flux during the soft/high state. We need high spectral resolution ultraviolet observations during the hard/low state to determine if there is a change in wind density between states.

Our determination of the mass-accretion rate can be considered as a positive check on the Hatchett-McCray models, as the Si IV line gave $L_x = 1.6 \times 10^{37}$ erg s $^{-1}$, and the model is subject to systematic uncertainties. However, this value of L_x is a factor of 3 lower than the best estimate of the accretion rate according to Bondi-Hoyle-Littleton spherical wind accretion. We suggest that some of the energy of accretion may go into powering the jet.

Our test of the dependence of our results on X-ray luminosity confirms the utility of our models and demonstrates that the wind outside the shadow zone is still sensitive to X-ray illumination, an arrangement which allows us to fit L_x as a free parameter in our model.

In future observations of the time-variability of the wind lines, the light travel-time effects may be used to advantage, as the wind may act as a “low-pass filter” to the X-ray observations, with the filter cutoff indicating the size of the ionized region (Kallman, McCray, & Voit 1987).

AH would like to acknowledge support from the REU program NSF grant 9731923 awarded to SAO. DG would like to acknowledge support provided by NASA through a grant (GO-9840) from the Space Telescope Science Institute, which is operated by the Association of Universities for Research in Astronomy, Incorporated, under NASA contract NAS5-26555. The X-ray results were provided by the ASM/RXTE teams at MIT and at the RXTE SOF and GOF at NASA’s GSFC. The contour graphs of ion fraction benefitted from the programming of Corey Casto, who helped increase the resolution of the contours.

REFERENCES

- Bautista, M.A., & Kallman, T.R. 2001, ApJS, 134, 139
- Bolton, C.T. 1972, Nature phys. Sci., 240, 124
- Bondi, H., & Hoyle, F. 1944, MNRAS, 104, 273
- Boroson, B.S., Kallman, T., Vrtilik, S.D., McCray, R., & Raymond, J. 1999, ApJ, 519, 191
- Brockopp, C. *et al.* 1999, A&A, 343, 861
- Cowley, A. 1992, ARA&A, 30, 287
- Davis, R., & Hartmann, L. 1983 ApJ, 270, 67
- Friend, D.B., & Cassinelli, J.P. 1986, ApJ, 303, 292
- Gies, D.R., & Bolton, C.T. 1986, ApJ, 304, 371
- Gies, D.R. *et al.* 2003, ApJ, 583, 424
- Gies, D.R. *et al.* 2007, ApJ, submitted
- Kallman, T.R., McCray, R., & Voit, G.M. 1987, ApJ, 317, 746
- Kimble, R.A., *et al.* 1998, SPIE, 3356, 188
- Lamers, H.J.G.L.M., Cerruti-Sola, M., & Perinotto, M. 1987, ApJ, 314, 726
- Lamers, H.J.G.L.M., Haser, S., de Koter, A., & Leitherer, C. 1999, ApJ, 516, 872
- Levine, A. M. *et al.* 1996, ApJL, 469, L33
- Marshall, H.L. *et al.* 2001, in Proc. Joint Workshop on X-ray Emission from Accretion onto Black Holes, ed. T. Yagoob, & J. Krolik, preprint (astro-ph/0111464).
- McCray, R., Kallman, T.R., Castor, J.I., & Olson, G.L. 1984, ApJ, 282, 245
- Miller, J.M. *et al.* 2002, ApJ, 578, 348
- Miller, J.M. *et al.* 2005, ApJ, 620, 398

- Nelder, J.A., & Mead, R. 1965, *Computer Journal*, 7, 308
- Ninkov, Z., Walker, G.A.H., & Yang, S. 1987, *ApJ*, 321, 425
- Schulz, N.S., Cui, W., Canizares, C.R., Marshall, H.L., Lee, J.C., Miller, J.M., Lewin, W. H. G. 2002, *ApJ*, 565, 1141
- Shapiro, S.L., & Teukolsky, S.A. 1983, *Black Holes, White Dwarfs, and Neutron Stars: The Physics of Compact Objects* (New York: John Wiley & Sons)
- Shaposhnikov, N. & Titarchuk, L. 2007 *ApJ*, 663, 445
- Sowers, J.W., Gies, D.R., Baguolo, W.G., Shafter, A.W., Wiemker, R., & Wiggs, M.S. 1998, *ApJ*, 506, 424
- Tarasov, A.E., Brocksopp, C., & Lyuty, V.M. 2003, *A&A*, 402, 237
- Treves, A. *et al.* 1980, *ApJ*, 242, 1114
- van Loon, J. Th., Kaper, L. & Hammerschlag-Hensberge, G. 2001, *A&A*, 375 498
- Verner, D.A., Barthel, P.D., & Tytler, D. 1994, *A&AS*, 108, 287
- Vrtilek, S.D. Boroson, B.S., Cheng, F.H., McCray, R., & Nagase, F. 1997, *ApJ*, 490, 377
- Wen, L., Cui, W., Levine, A.M., & Bradt, H.V. 1999, *ApJ*, 525, 986
- Wilms, J., Nowak, M. A., Pottschmidt, K., Pooley, G. G., & Fritz, S. 2006, *A&A*, 447, 245
- Wojdowski, P.S., Liedahl, D.A., Sako, M., Kahn, S.M., & Paerels, F. 2003, *ApJ*, 582, 959
- Woodgate, B.E., *et al.* 1998, *PASP*, 110, 1183
- Ziolkowski, J. 2005 *MNRAS*, 358, 851

Table 1: Log of Observations

Obs. ID:			Exposure	Orbital
HST Archive ID	Obs. Start Time	MJD	(s)	Phase*
Dataset 1: O8HD1010	2002-06-24 18:10:02	52449.757	2676.00	0.55
Dataset 2: O8HD1020	2002-06-24 19:36:41	52449.817	2172.00	0.56
Dataset 3: O8HD2010	2002-06-27 16:39:48	52452.694	2172.00	0.07
Dataset 4: O8HD2020	2002-06-27 18:06:34	52452.754	2676.00	0.08
Dataset 5: O8NX1010	2003-07-05 04:27:23	52825.185	2147.00	0.59
Dataset 6: O8NX1020	2003-07-05 05:51:58	52825.244	2675.00	0.60
Dataset 7: O8NX2010	2003-07-07 04:27:47	52827.185	2147.00	0.95
Dataset 8: O8NX2020	2003-07-07 05:53:29	52827.245	2675.00	0.96

*Phase computed at center of observation.

Table 2: Line identifications for the spectrum of Figure 4.

Laboratory		Transition	Comment
Line ID	Wavelength (\AA)		
Ly α	1215.670	1-2 $_{1/2-*}$	saturated
N V	1238.821	$^2\text{S}-^2\text{P}^o$ $_{1/2-3/2}$	saturated
N V	1242.804	$^2\text{S}-^2\text{P}^o$ $_{1/2-1/2}$	saturated
Si II	1260.422	$^2\text{P}^o-^2\text{D}$ $_{1/2-3/2}$	
O I	1302.168	$^3\text{P}-^3\text{S}^o$ $_{2-1}$	weak,blended with Si I I
O I	1304.858	$^3\text{P}-^3\text{S}^o$ $_{1-1}$	weak,blended with Si II
Si II	1304.370	$^2\text{P}^o-^2\text{S}$ $_{1/2-1/2}$	weak,blended with O I
Si II	1309.276	$^2\text{P}^o-^2\text{S}$ $_{3/2-1/2}$	weak,blended with O I
C II	1334.532	$^2\text{P}^o-^2\text{D}$ $_{1/2-3/2}$	weak
C II	1335.663	$^2\text{P}^o-^2\text{D}$ $_{3/2-3/2}$	weak
Si IV	1393.755	$^2\text{S}-^2\text{P}^o$ $_{1/2-3/2}$	
Si IV	1402.770	$^2\text{S}-^2\text{P}^o$ $_{1/2-1/2}$	
Si II	1526.707	$^2\text{P}^o-^2\text{S}$ $_{1/2-1/2}$	
Si II	1533.431	$^2\text{P}^o-^2\text{S}$ $_{3/2-1/2}$	
C IV	1548.203	$^2\text{S}-^2\text{P}^o$ $_{1/2-3/2}$	
C IV	1550.777	$^2\text{S}-^2\text{P}^o$ $_{1/2-1/2}$	
He II	1640.420	2-3 $_{*-}$	weak
Al II	1670.787	$^1\text{S}-^1\text{P}^o$ $_{0-1}$	

Table 3: Model Parameters

Symbol	Adopted value	Meaning	Comments
i	40°	Orbital inclination	$< 20 - 67^\circ$ (Gies <i>et al.</i> 2003, Tarasov <i>et al.</i> 2003; Wen <i>et al.</i> 1999; Herrero <i>et al.</i> 1995; Friend & Cassinelli 1986; Davis & Hartmann 1983)
R_O	1.5×10^{12} cm	Radius of O star	1.23×10^{12} cm (Davis & Hartmann 1983) $1.2 - 1.6 \times 10^{12}$ cm (Gies & Bolton 1986)
R_{orbit}	$2.0 R_O$	Semimajor axis	$2.4 R_O$ (Davis & Hartmann 1983)
$V_{\text{sin}i}$	94 km s^{-1}	(Projected rotation velocity)	94.3 ± 5 (Ninkov <i>et al.</i> 1987), 96 (Gies & Bolton 1986)
v_{sys}	0	Systemic velocity	$0_{-9}^{+6} \text{ km s}^{-1}$ (Ninkov <i>et al.</i> 1987)
a_C	3.6×10^{-4}	Carbon abundance	solar from Verner <i>et al.</i> 1994
a_N	1.1×10^{-4}	Nitrogen abundance	solar from Verner <i>et al.</i> 1994
a_{Si}	3.5×10^{-5}	Silicon abundance	solar from Verner <i>et al.</i> 1994

Table 4: Best-fit values for free parameters for Cygnus X-1 P Cygni line fits

Symbol	Fitted value (Si IV, CIV, NV)	Definition*	Comments
β	0.748 ± 0.003	Wind acceleration	Fit to Si IV, then fixed
τ_*	$(0.436 \pm 0.007, 0.88 \pm 0.03, 0.63 \pm 0.05)$	Optical depth of stellar absorption line	
τ_{wind}	$(12.7 \pm 0.2, 25.2 \pm 0.1, 7.8 \pm 1.0)$	Wind total depth	
v_∞	$(1420 \pm 10, 1330 \pm 30, 1430) \text{ km s}^{-1}$	Wind terminal velocity	2300 km s^{-1} (Davis & Hartmann 1983), Frozen for NV
v_{turb}	$(160 \pm 10, 292 \pm 1, 200) \text{ km s}^{-1}$	Wind microturbulence	Frozen for NV
α_1	$(-0.31 \pm 0.03, 0.32 \pm 0.01, 0.66 \pm 0.10)$	Wind opacity exponent	
α_2	$(0.89 \pm 0.06, 0.140 \pm 0.004, 0.80 \pm 0.01)$	Wind opacity exponent	
$L_{\text{x},38}/\dot{M}_{-6}$	$(0.033 \pm 0.001, 0.38 \pm 0.01, 0.12 \pm 0.01)$	Ratio, X-ray luminosity ($10^{38} \text{ erg s}^{-1}$) to wind mass loss ($10^{-6} M_\odot \text{ yr}^{-1}$)	
\dot{M}_{-6}	$(4.8 \pm 0.3, 4.8 \pm 0.1, 6.7 \pm 0.2)$	Wind mass loss rate ($10^{-6} M_\odot \text{ yr}^{-1}$)	
χ_ν^2	$(3.0, 5.8, 1.3)$	Goodness of fit	
ν	$(933, 596, 585)$	Degrees of freedom	

*From Lamers, Cerruti-Sola, & Perinotto (1987).

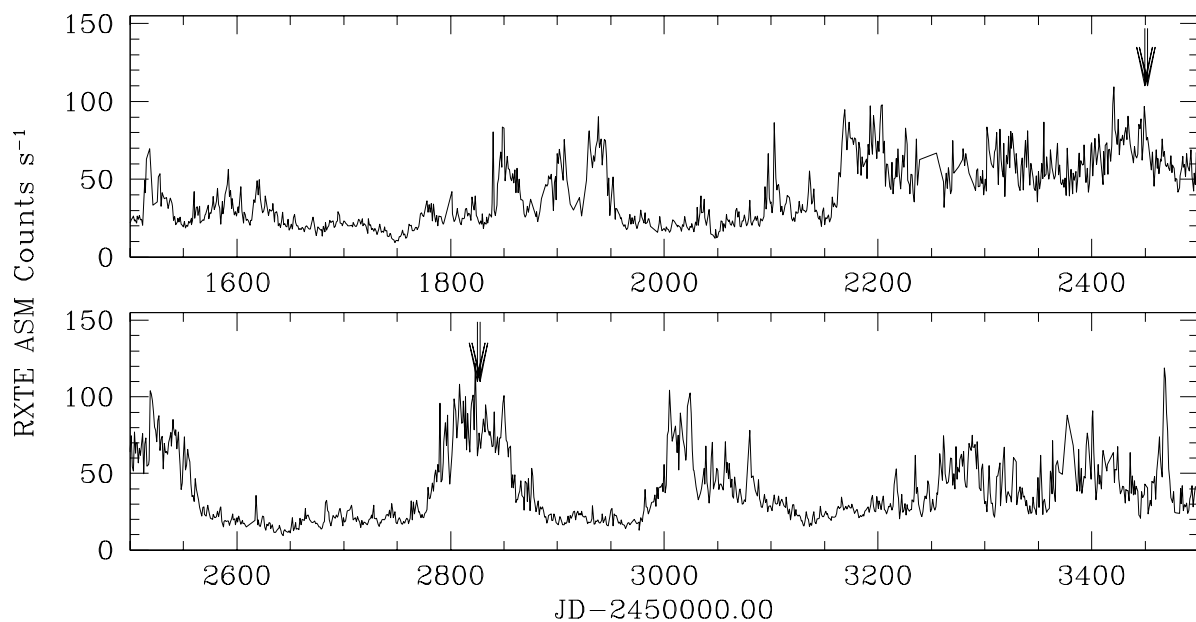


Fig. 1.— One day averages of the flux observed from Cyg X-1 with the All-Sky Monitor on board the Rossi X-Ray Timing Explorer. Arrows indicate the times of the HST/STIS observations.

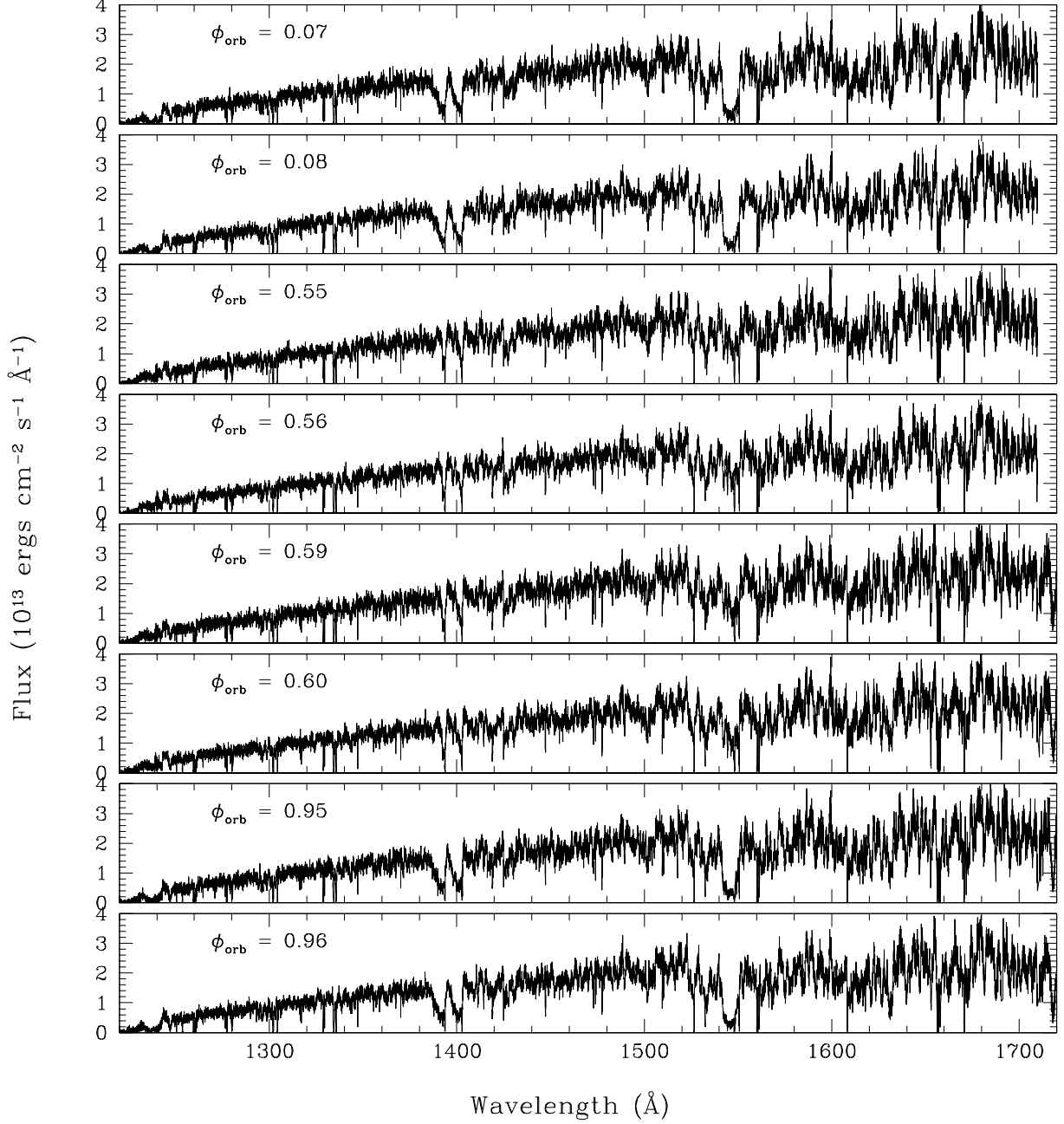


Fig. 2.— Unsmoothed, raw, HST/STIS data of Cygnus X-1 stacked with increasing orbital phase, regardless of epoch.

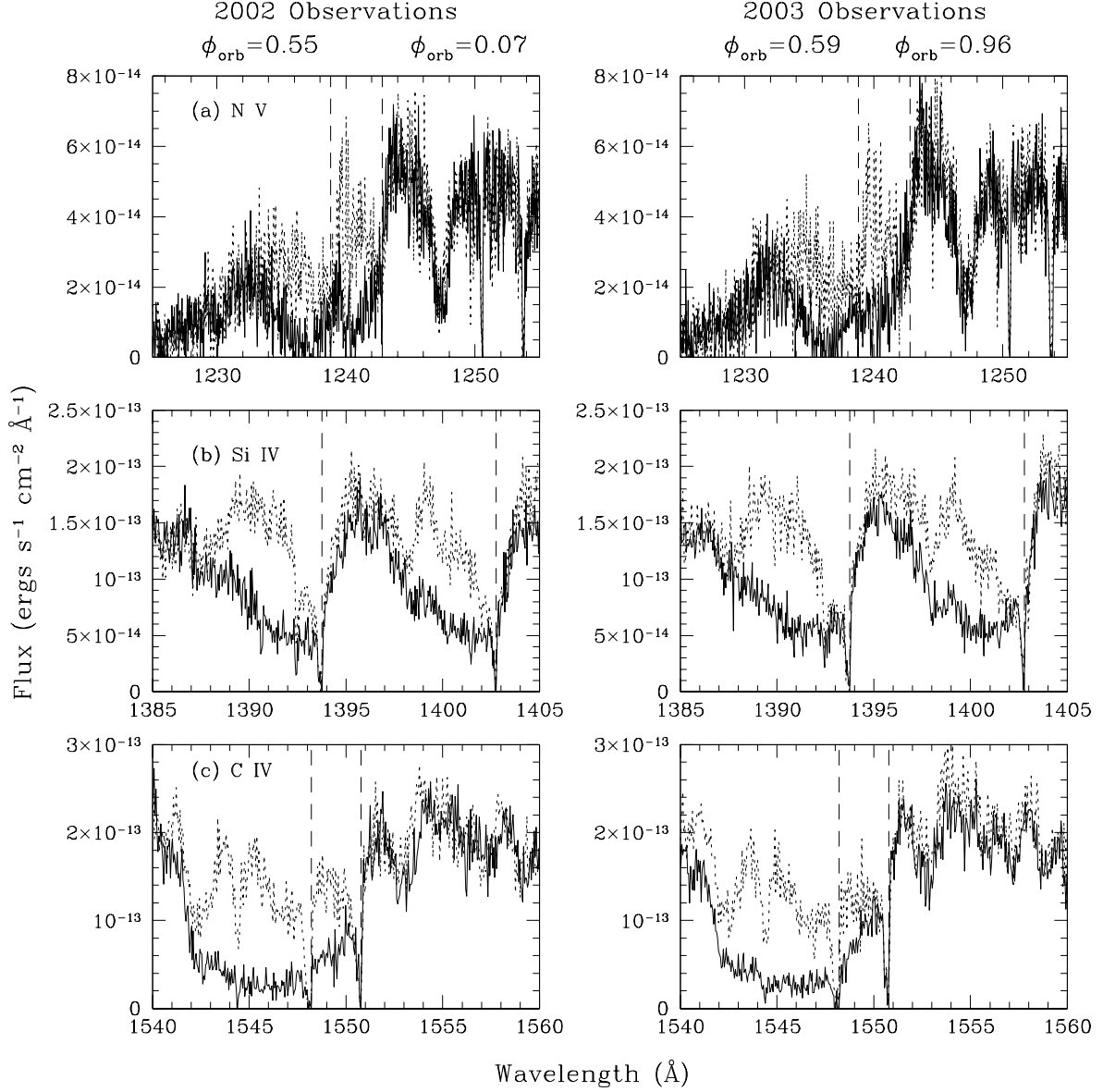


Fig. 3.— STIS observations of Cyg X-1 taken roughly a year apart showing enhanced absorption at orbital phases when the X-ray source is behind the companion star (phase 0.0; solid lines) and illustrating the stability of the absorption change as a function of orbital phase. Narrow features are interstellar. Black dashed lines indicate the laboratory wavelengths of transitions identified in Table 2.

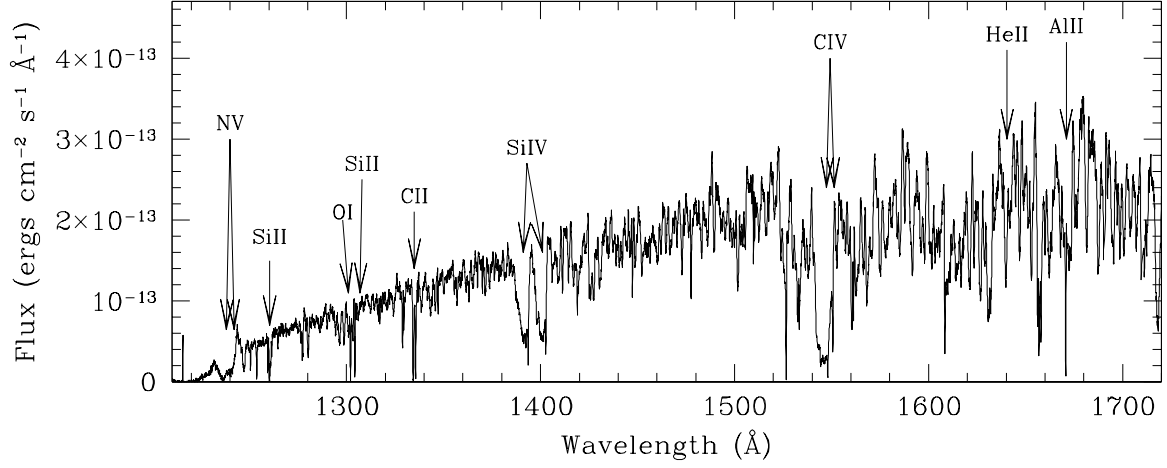


Fig. 4.— A Cyg X-1 STIS spectrum at phase 0.96 with major spectral features indicated. The data have been smoothed with a 7-point boxcar function to better show the features of interest. Sharp features are interstellar absorption lines.

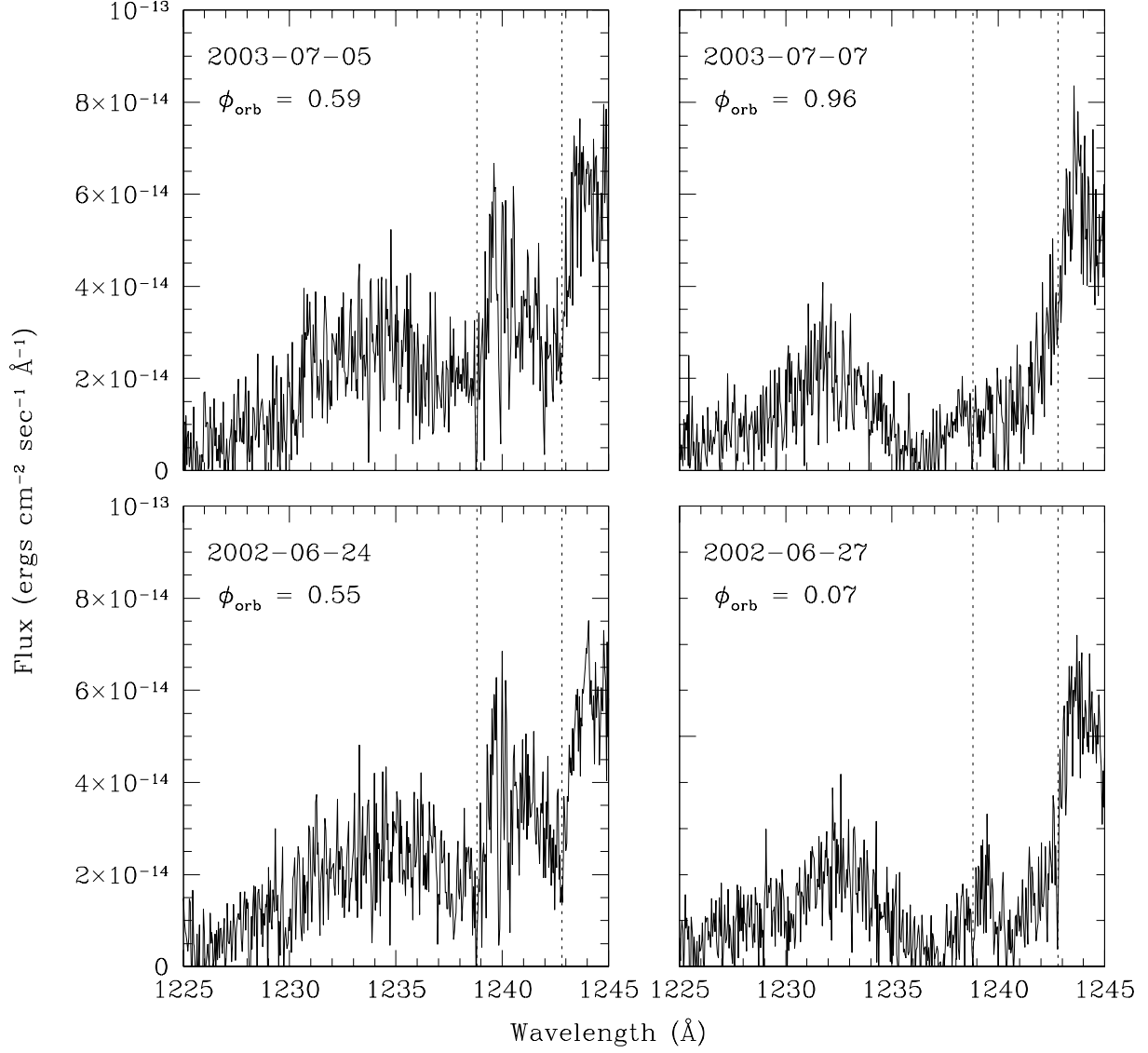


Fig. 5.— Spectra of the N V line at two different orbital phases and two different epochs. The dashed lines indicate the laboratory wavelengths for transitions listed in Table 2.

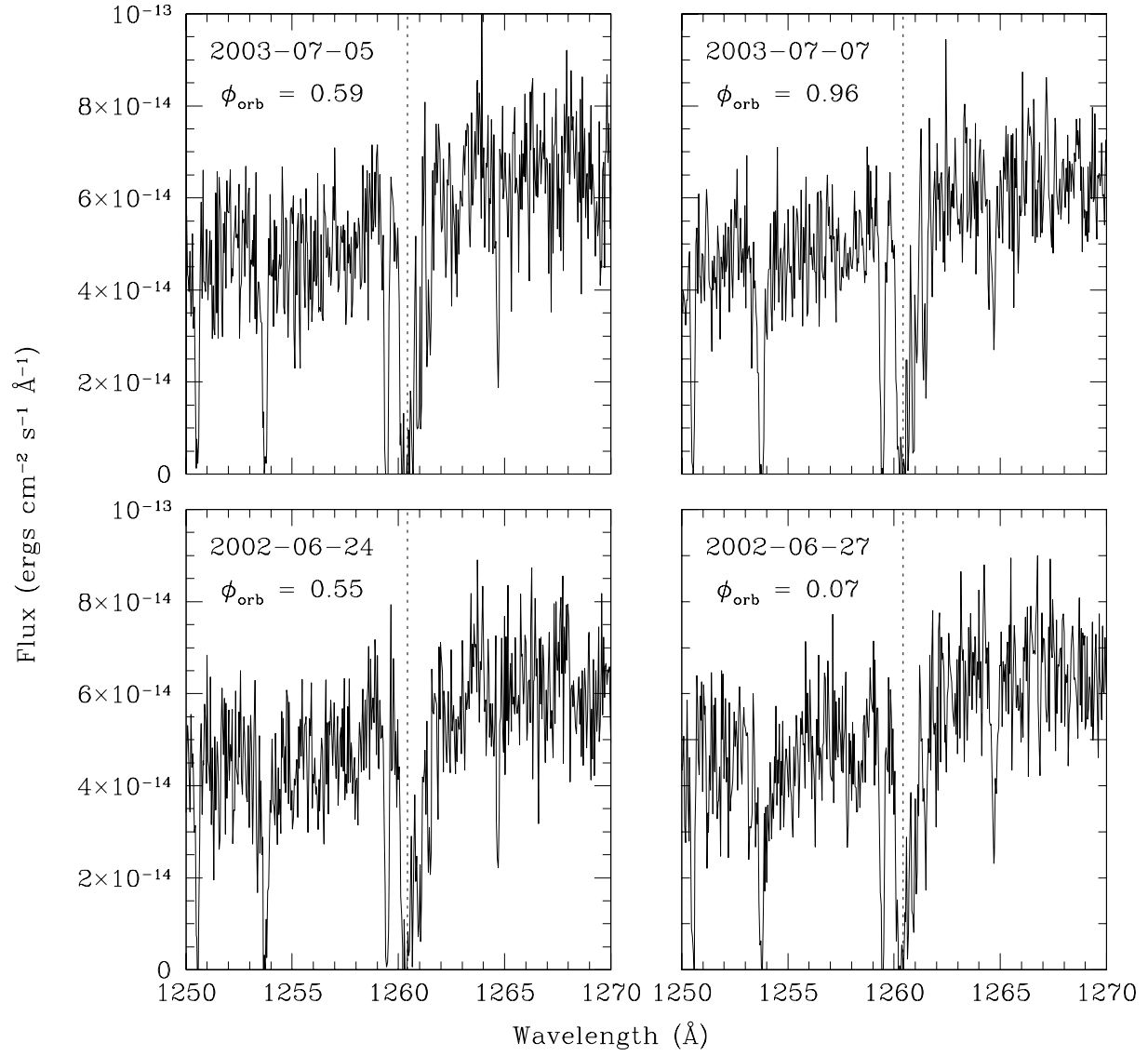


Fig. 6.— As in figure 5 for Si II

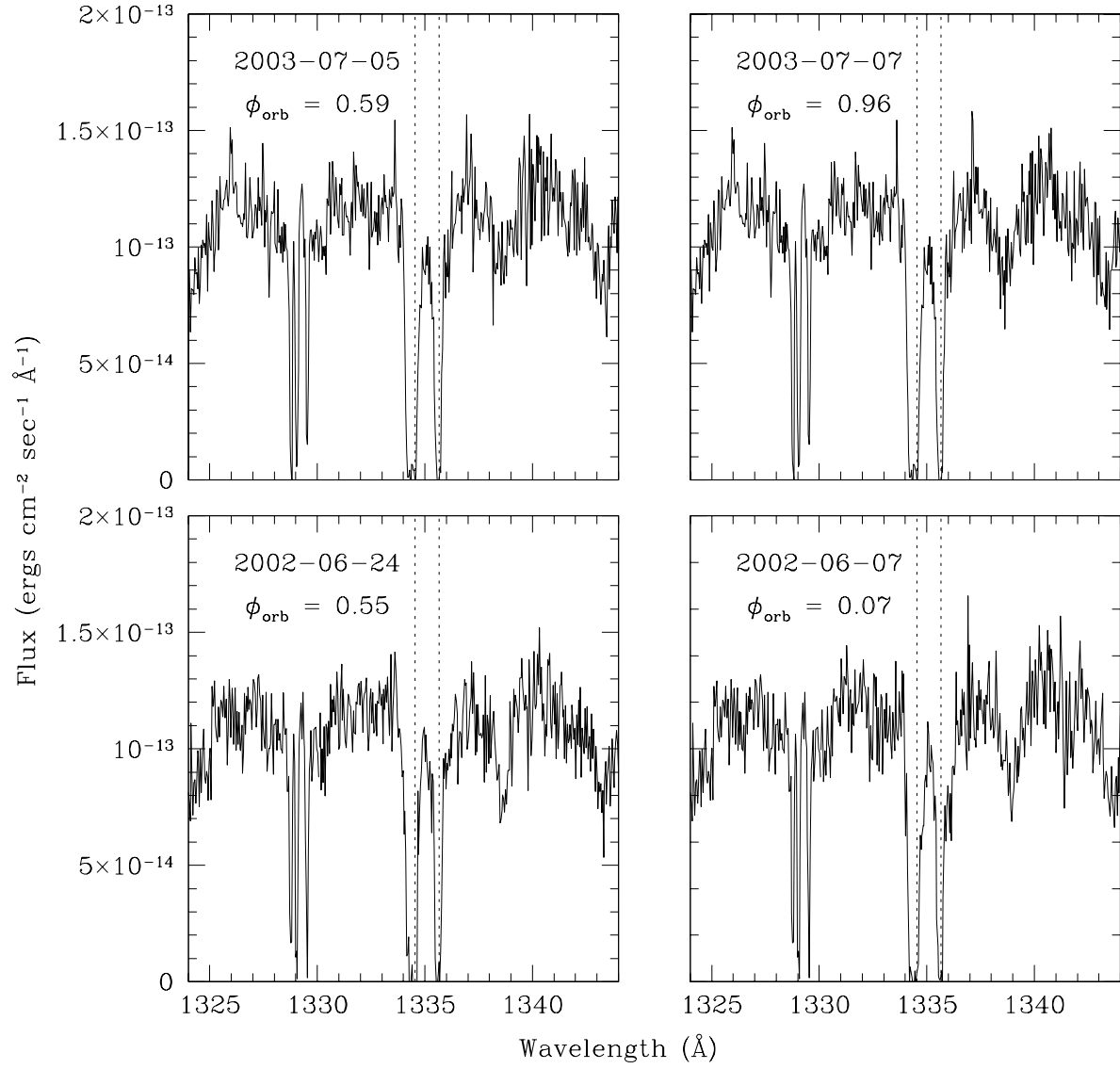


Fig. 7.— As in figure 5 for C II

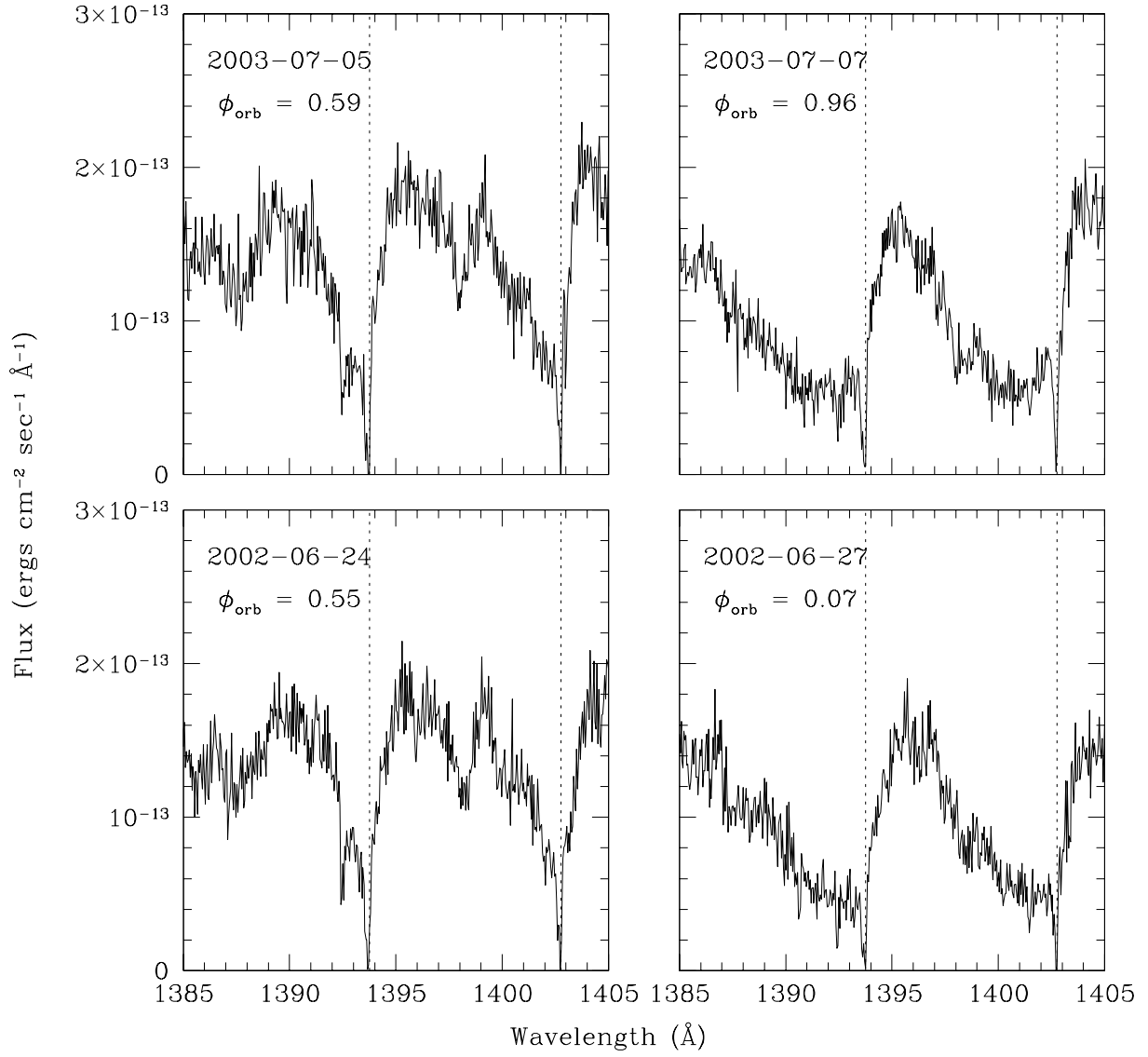


Fig. 8.— As in figure 5 for Si IV

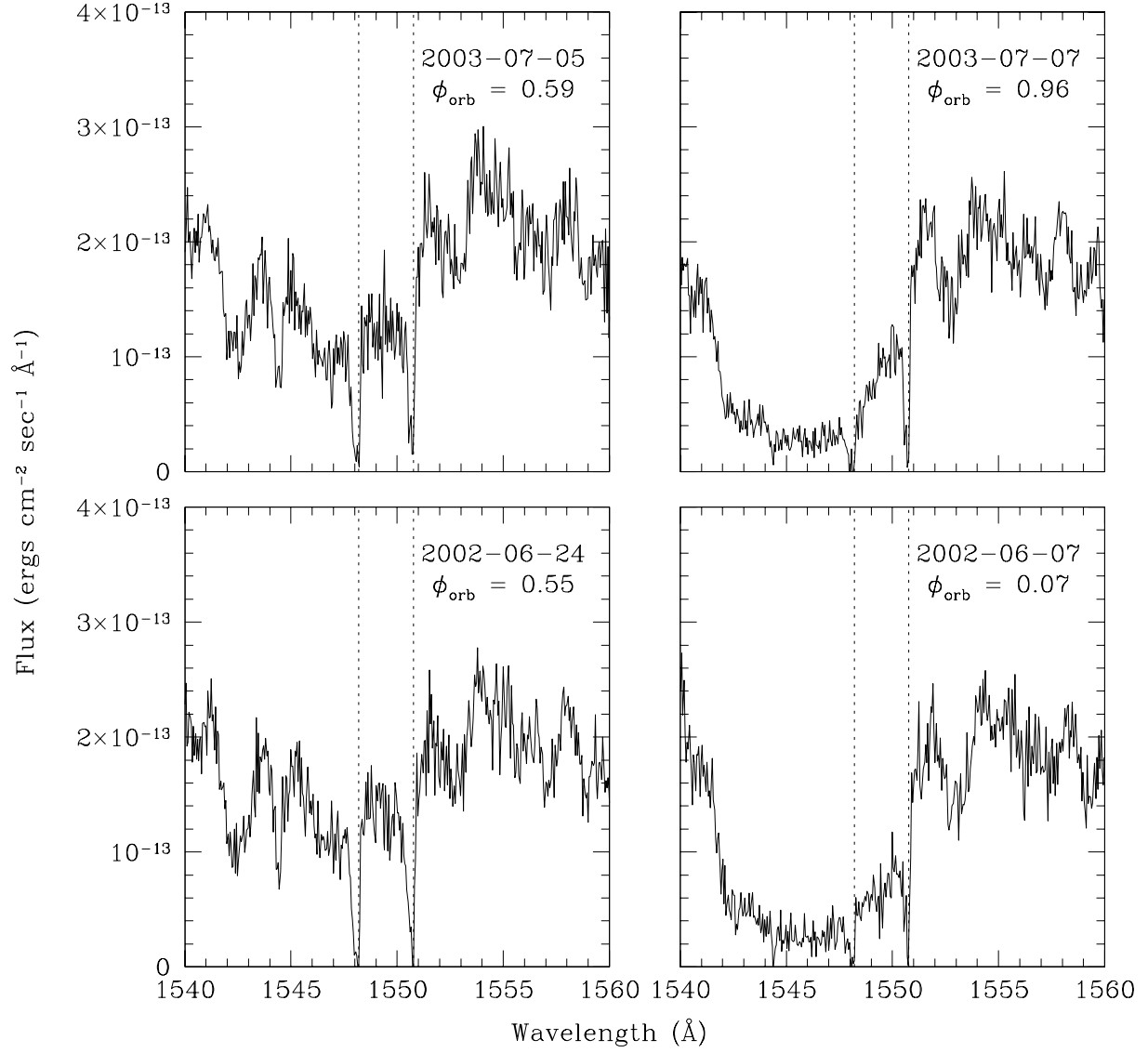


Fig. 9.— As in figure 5 for C IV

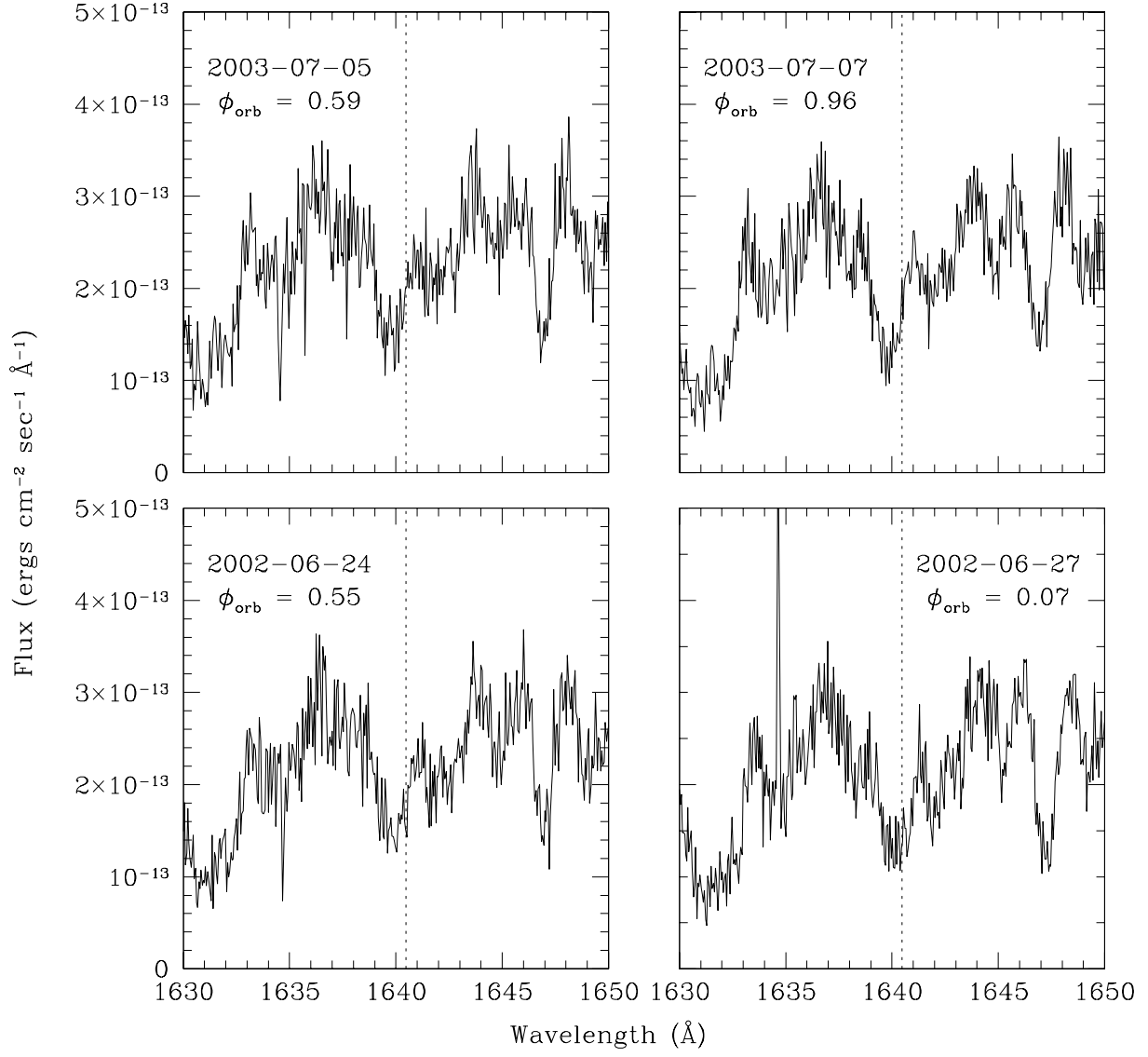


Fig. 10.— As in figure 5 for HeII

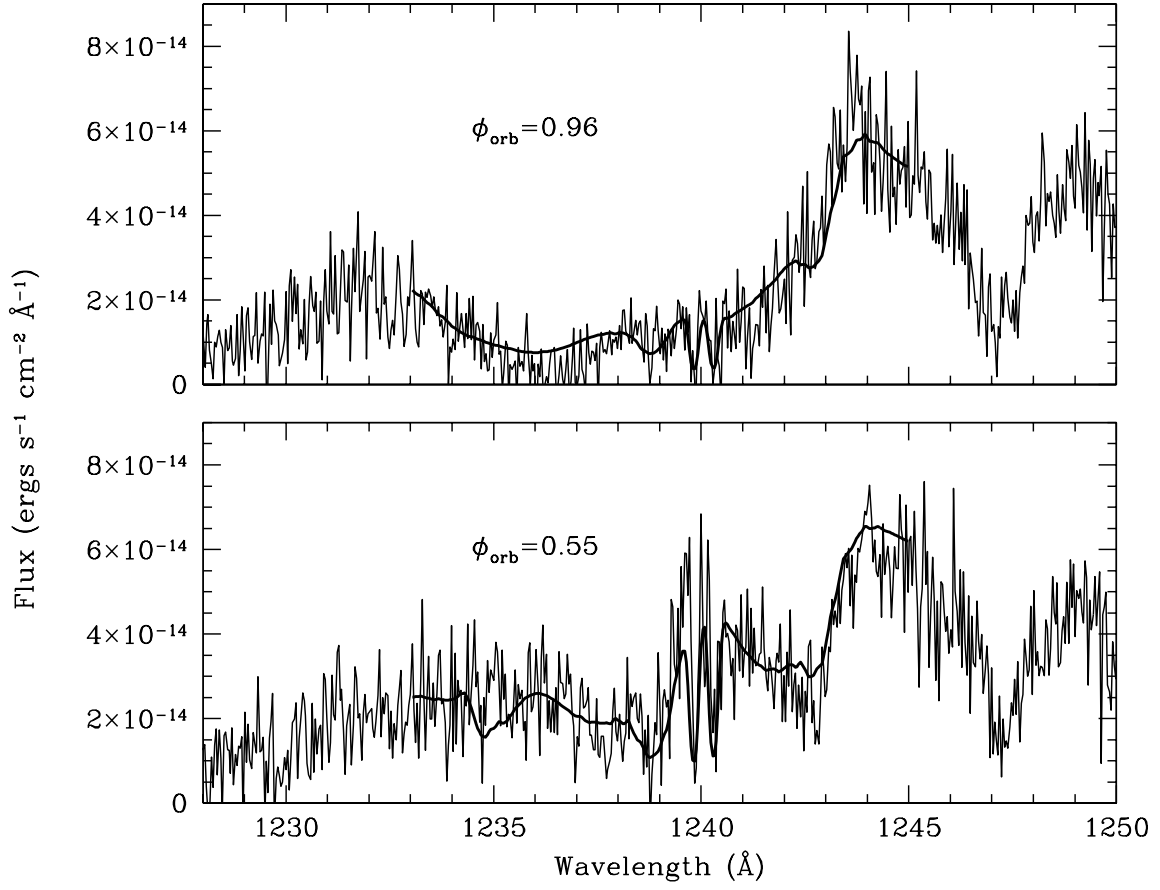


Fig. 11.— Closeup of Cyg X-1 N V line profiles. The blue line depicts a model computed using the SEI method (Lamers, Cerruti-Sola, & Perinotto 1987), using a wind velocity law given by $v_{\infty} (1 - 1/r)^{\beta}$.

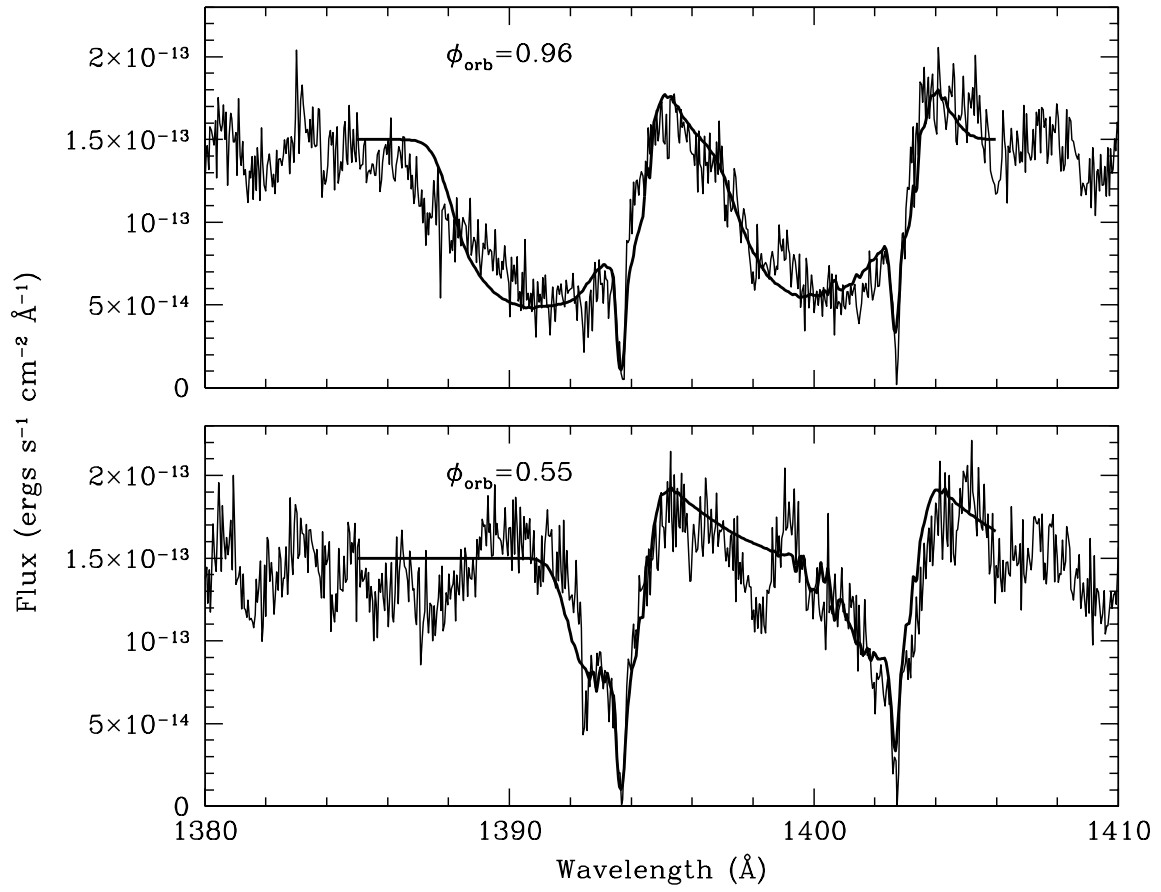


Fig. 12.— As in Fig. 11 for Si IV.

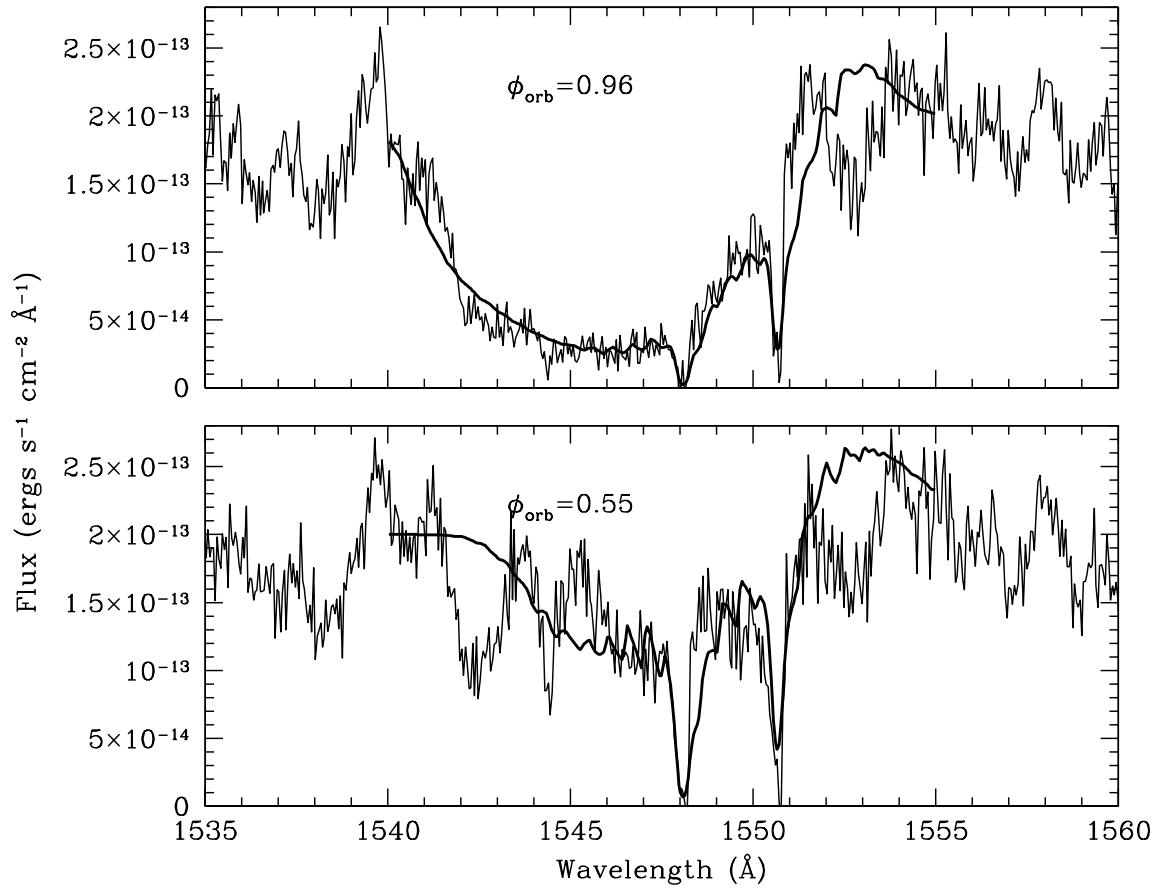


Fig. 13.— As in Fig. 11 for C IV.

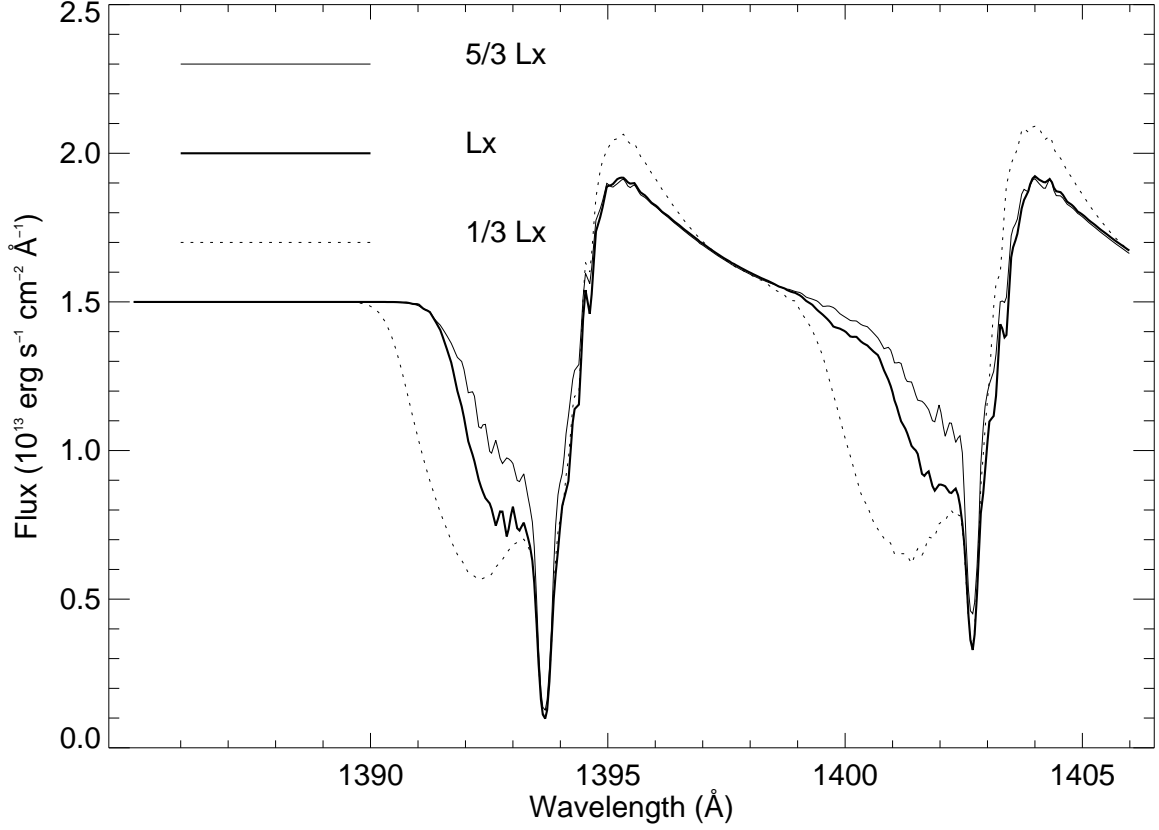


Fig. 14.— The response of the wind-formed P Cygni lines to X-ray luminosities of $1/3L_x$, L_x , and $5/3L_x$ (dotted, bold, and regular thickness, respectively). All other parameters are as assumed for the best fit to the Si IV lines. This figure shows the model at $\phi=0.55$ and ignores the effects of light travel-time, which would tend to decrease the change in the line with changing X-ray luminosity.

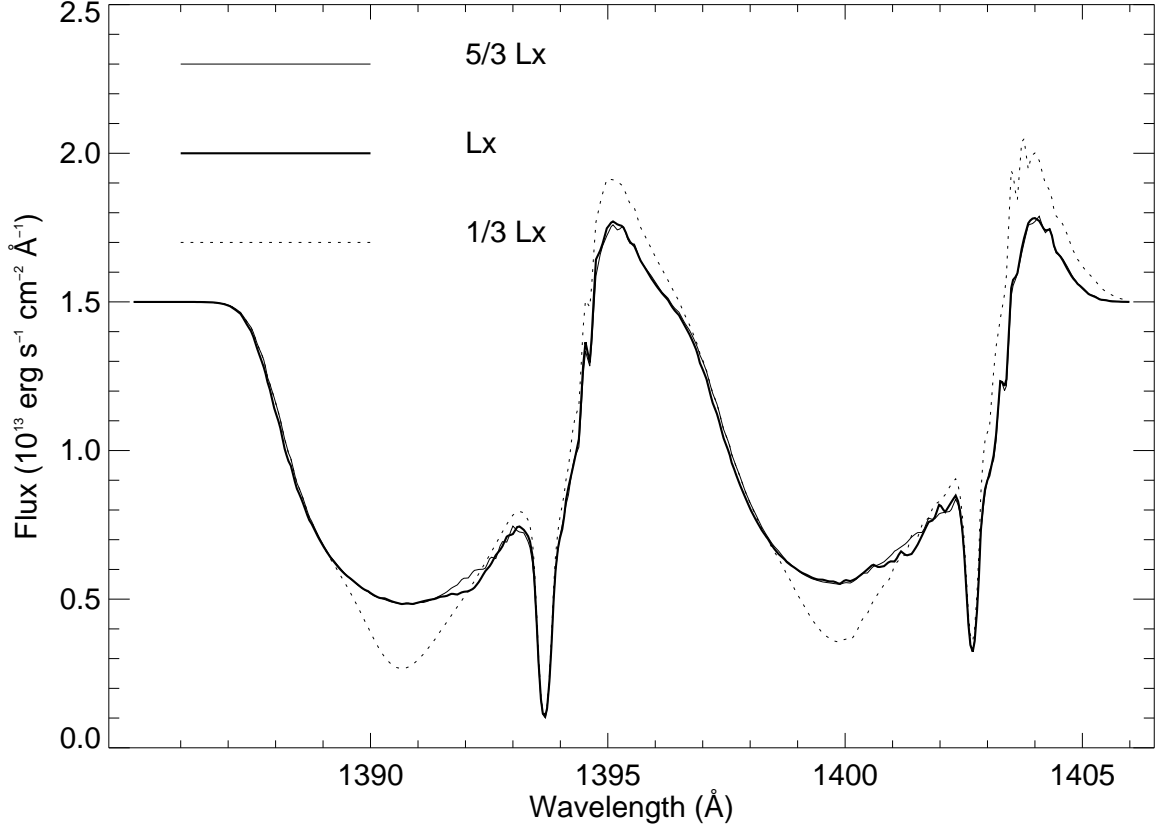


Fig. 15.— The response of the wind-formed P Cygni lines to X-ray luminosities of $1/3L_x$, L_x , and $5/3L_x$ (dotted, bold, and regular thickness, respectively). All other parameters are as assumed for the best fit to the Si IV lines. This figure shows the model at $\phi=0.96$ and ignores the effects of light travel-time, which would tend to decrease the change in the line with changing X-ray luminosity.

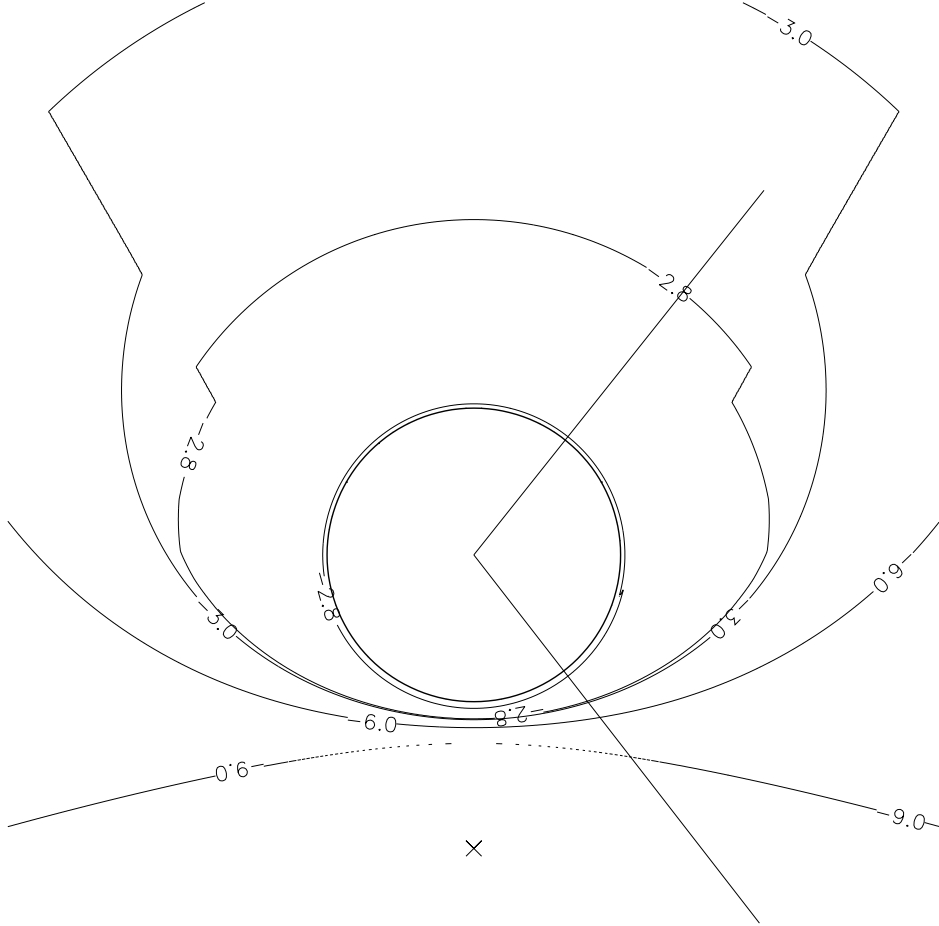


Fig. 16.— Contours of Log_{10} of Si IV abundance outside of the shadow region. We assume the X-ray luminosity is $(1/3)1.6 \times 10^{37} \text{ erg s}^{-1}$, and that all other parameters have their best-fit values. We include only ionization from the black hole and not the ambient ionization of the wind. The circle represents the supergiant and the X the position of the compact source.

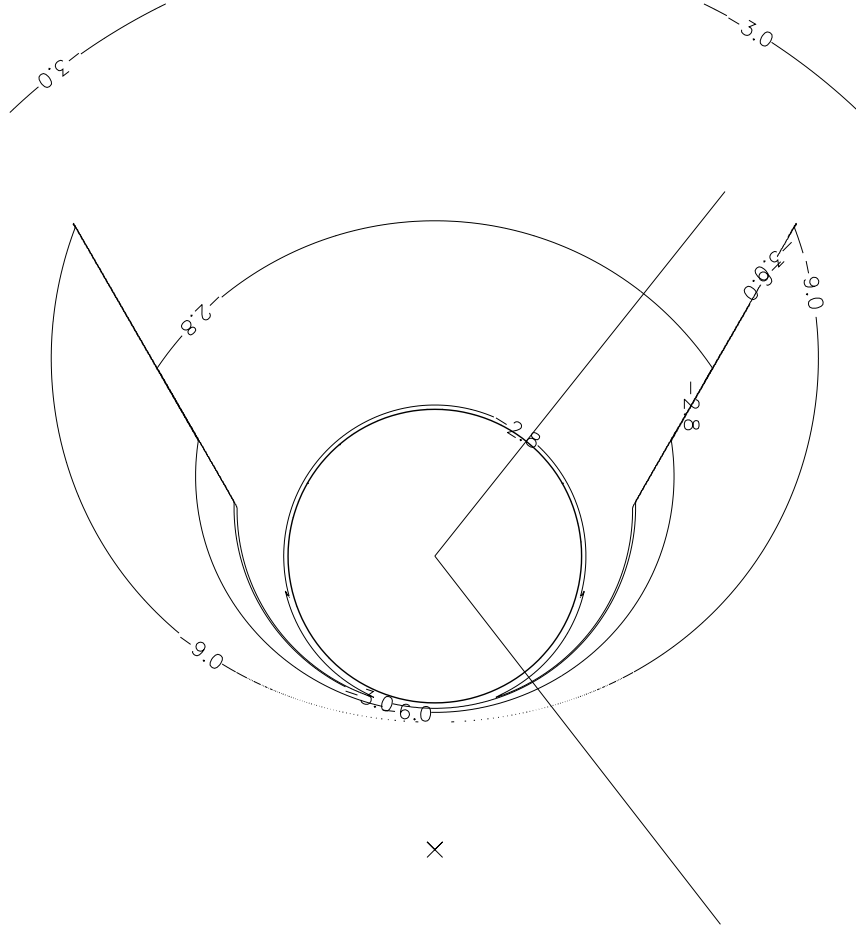


Fig. 17.— Contours of Log_{10} of Si IV abundance outside of the shadow region. We assume the X-ray luminosity is $1.6 \times 10^{37} \text{ erg s}^{-1}$, and that all other parameters have their best-fit values. We include only ionization from the black hole and not the ambient ionization of the wind.

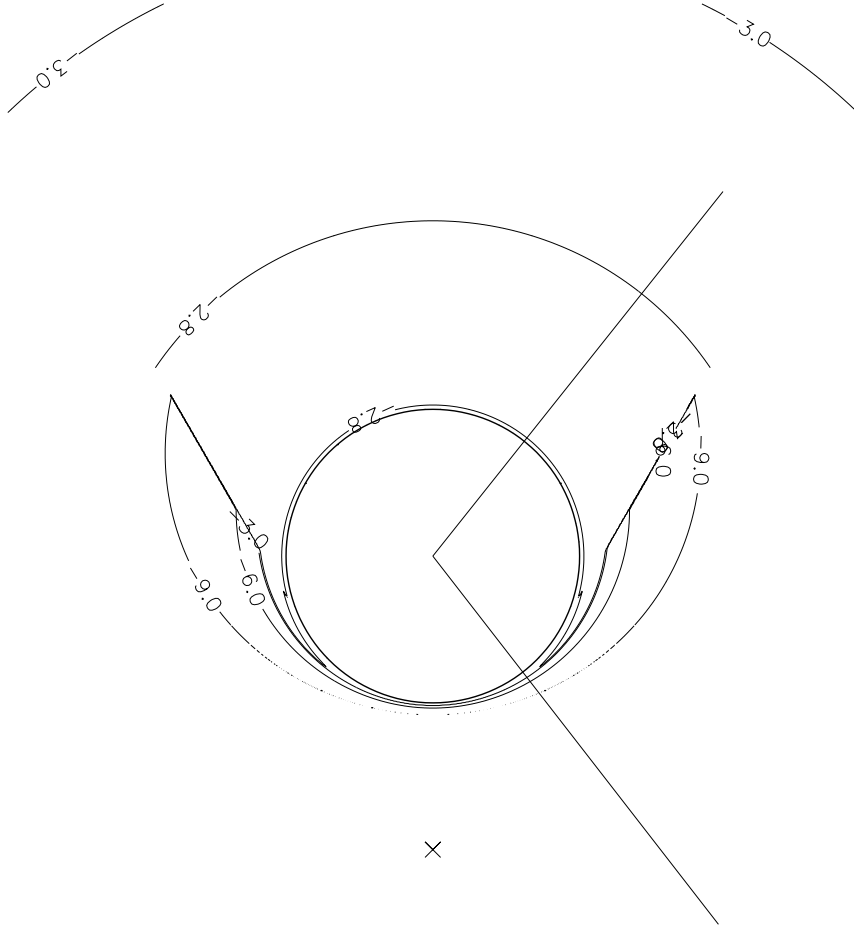


Fig. 18.— Contours of Log_{10} of Si IV abundance outside of the shadow region. We assume the X-ray luminosity is $(5/3)1.6 \times 10^{37} \text{ erg s}^{-1}$, and that all other parameters have their best-fit values. We include only ionization from the black hole and not the ambient ionization of the wind.

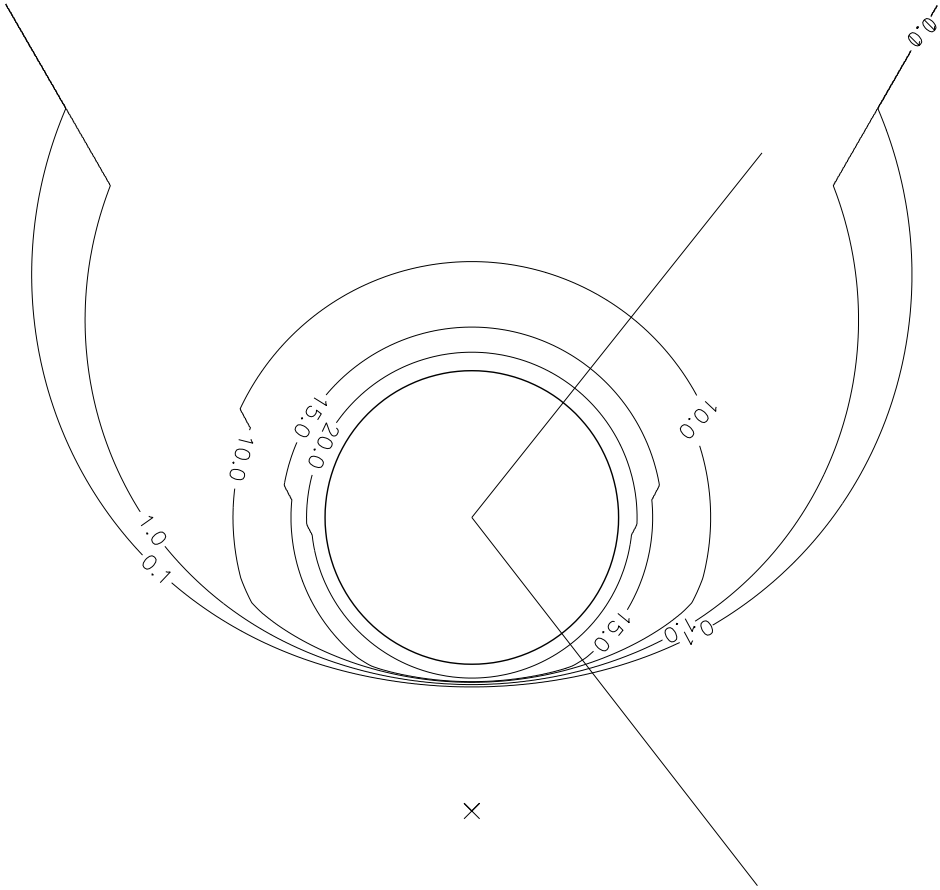


Fig. 19.— Contours of radial optical depth τ , given the X-ray luminosity is $(1/3)1.6 \times 10^{37} \text{ erg s}^{-1}$.

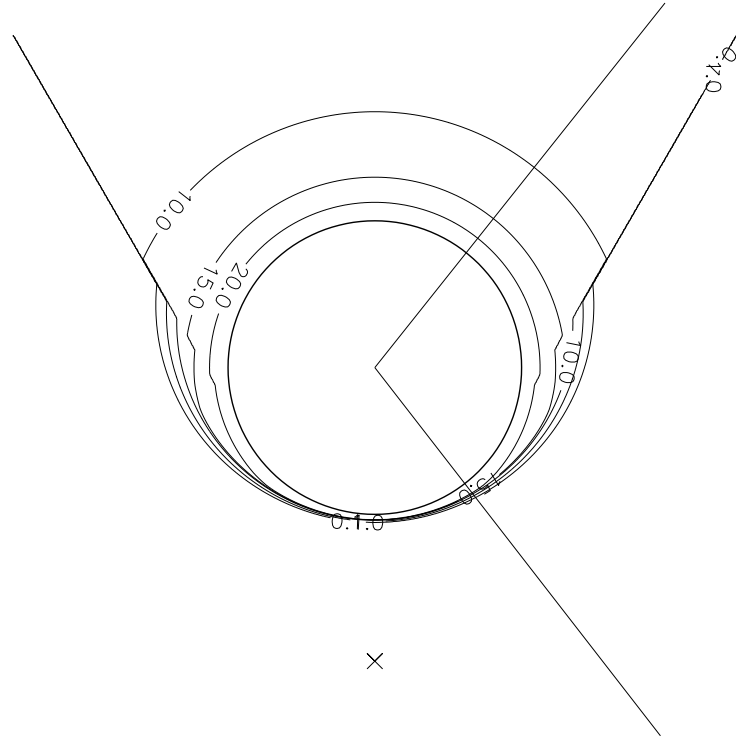


Fig. 20.— Contours of radial optical depth τ , given the X-ray luminosity is $1.6 \times 10^{37} \text{ erg s}^{-1}$.

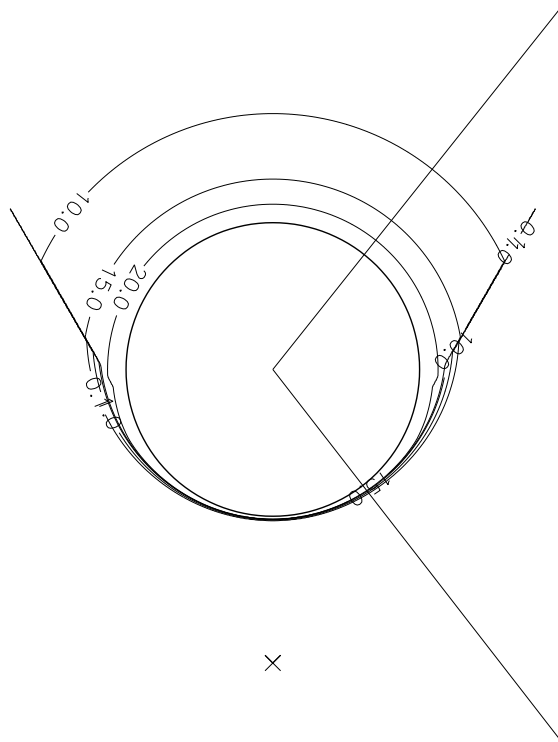


Fig. 21.— Contours of radial optical depth τ , given the X-ray luminosity is $(1/3)1.6 \times 10^{37} \text{ erg s}^{-1}$.